Study of Dielectric Behavior and Electrical Properties of Hematite α-Fe₂O₃ Doped with Zn

M. V. Nikolic[1*], **M. P. Slankamenac**[2], **N. Nikolic**[1], **D. L. Sekulic**[2], **O. S. Aleksic**[1], **M. Mitric**[3], **T. Ivetic**[4], **V. B. Pavlovic**[4], **P. M. Nikolic**[4]

[1]Institute for Multidisciplinary Research, University of Belgrade, Kneza Viseslava 1, 11000 Beograd, Serbia
[2]Faculty of Technical Sciences, University of Novi Sad, 21000 Novi Sad, Serbia
[3]The "Vinca" Institute of Nuclear Science, Laboratory for Theoretical Physics and Physics of Condensed Matter, PO Box 522, 11001 Beograd, Serbia
[4]Institute of Technical Sciences of SASA, Knez Mihailova 35, 11000 Beograd, Serbia

Abstract:

The effects of Zn-doping on the dielectric behavior and electrical properties of bulk α-Fe₂O₃ have been studied. X-ray diffraction analysis revealed the presence of two phases in all samples: hematite and spinel ZnFe₂O₄, with the amount of spinel phase increasing with increasing Zn content. Scanning electron microscopy analysis combined with energy dispersive X-ray spectroscopy showed that the Zn-bearing phase occurred in the form of individual spinel ZnFe₂O₄ grains in a hematite matrix. DC conductivity was measured in the temperature range 25-225ᵒC (298-498 K). Impedance spectroscopy measurements in the same temperature range were carried out in the frequency range 100Hz to 10 MHz. Increase in the Zn content resulted in increased electrical conductivity and higher values of the dielectric constant. The resistance and capacitance of grains and grain boundaries were analyzed by modeling the experimental results using an equivalent circuit.

Keywords: X-ray diffraction; Scanning electron microscopy; Dielectric response; Electrical transport.

1. Introduction

Hematite (α-Fe₂O₃) is a widely spread, cheap, non-toxic semiconductor stable in aqueous conditions with a band gap of 2.1 eV enabling absorption of a good deal of the solar spectrum [1-3]. It is widely used in catalysts, pigments and sensors [1-3]. Doping of pure hematite has been widely investigated, mainly with the purpose of improving its photoelectrochemical properties. Substitutional doping with Al [4], Mo, Cr [5], Si, Ti [6,7] and Zn [8] among other atoms has been reported. In most cases any improvement in performance has been attributed to improved conductivity due to a preferential ordering of crystallites or lattice distortions [4]. A combinatorial investigation of the effects of incorporation of Ti, Si and Al was studied in [9]. Electronic and magnetic effects of 3*d* transition metal doped α-hematite were studied in [10,11]. Interest in metal oxides and

_____

[*] **Corresponding author**: mariav@rcub.bg.ac.rs

especially hematite as candidates for photoelectrochemical solar cells has remained with the advent of nanotechnology [12].

Velev et al [11] showed that Zn substitutes as Zn^{2+} and its effect on the electronic properties of hematite would be the generation of a hole in the oxygen valence band. The extra hole from Zn is located on the neighbouring O sites forming an acceptor level just below the Fermi energy. As this hole is relatively delocalized this provides good hope for reasonably high conductivity. According to Ingler et al [8] pure hematite lacked adequate conductivity and the presence of Zn in the form of $ZnFe_2O_4$ improved magnetic and conductive properties. $ZnFe_2O_4$, a narrow band gap semiconductor (1.9 eV) has been used as a catalyst in photocatalytic degradation of pollutants [13]. $ZnFe_2O_4/\alpha-Fe_2O_3$ hollow nanospheres were synthesized recently by Shen et al [14] showing promising photo-absorbance properties.

In this work we have investigated the effect of Zn doping on electrical properties of bulk $\alpha-Fe_2O_3$ in order to get a better insight into how increased Zn presence resulting in the formation of spinel $ZnFe_2O_4$ influences dielectric properties, grain and grain boundary phenomena and the global electrical response.

2. Experimental

Hematite powder (purity 99.98%) was doped with zinc in fraction of 1, 2, 5 and 10 wt.% ZnO (purity 99.99%) and homogenized in a planetary ball mill for 15 minutes. Green samples 10 mm in diameter were sintered in the temperature range 900-1200°C for two hours.

XRD analysis of sintered samples of Zn doped Fe_2O_3 was performed on a Philips PW1050 diffractometer with a step scan of 0.02 s and holding time of 14 s. Unit cell parameters were calculated by Le Bail full pattern profile fitting [15] using the FullProf software suite [16]. Sample morphology was analyzed using scanning electron microscopy (JEOL JSM 6390 LV and JEOL JSM 6610LV) and energy dispersive X-ray spectroscopy.

Samples used for electrical conductivity measurements were prepared in the form of a sandwich electrode structure. Silver coatings were used as electrodes (ohmic contact). Electrical DC/resistivity/conductivity in the temperature range 25-225°C was measured on a High Resistance Meter (HP 4329A). Impedance measurements were carried out in the frequency range 100 Hz to 10 MHz on a HP-4194A impedance/gain-phase analyzer using a HP-16047A test fixture in the temperature range 25-225°C. A personal computer with in-house built software was used for acquisition of measured data.

## 3. Results and Discussion
3.1 Structural characterization

X-ray diffractograms of Zn doped Fe_2O_3 are shown in fig. 1 showing the presence of two phases in all samples: hematite ($\alpha-Fe_2O_3$) and spinel $ZnFe_2O_4$. The amount of spinel phase increased with increasing Zn content. Lattice parameters determined using LeBail full pattern profile fitting of both hematite and $ZnFe_2O_4$ phases are given in table I. This is in accordance with Ingler et al [8] who analyzed Zn doped hematite films and found that all zinc was identified in the form of $ZnFe_2O_4$.

The presence of two phases can also be noted in SEM micrographs. At lower sintering temperatures, the sintering process is in the initial stage, open porosity is present (fig. 2a). Sintering of Fe_2O_3 and formation of the spinel phase between Fe_2O_3 grains and ZnO grains proceeded at different sintering rates, thus resulting in the formation of cracks. At higher sintering temperatures the sintering process is in the final stage, grain growth is noticeable and we can note two distinct phases with different grain size for samples with the

_____

highest amount of Zn (fig. 2b). Backscatter imaging also revealed the presence of two phases. EDS analysis confirmed the presence of two phases. An example of compositions of both phases present in samples with 5 and 10 wt.% ZnO taken in different sites of interest on the analyzed samples are given in table II. X-ray distribution maps of constituent elements for α-Fe_2O_3 doped with 5 and 10 wt.% ZnO are shown in fig. 3. The X-ray map for Zn revealed that the Zn-bearing phase, $ZnFe_2O_4$ occurs in the form of individual grains in a hematite matrix. This is in accordance with obtained SEM micrographs (fig. 2b) where larger $ZnFe_2O_4$ spinel grains are locally interconnected and surrounded by smaller hematite grains.

Tab. I Unit cell parameters for two-phase system hematite and $ZnFe_2O_4$.

| Sample	Hematite		$ZnFe_2O_4$
	a [Å]	c [Å]	a [Å]
α-Fe2O3+1%ZnO	5.03775(8)	13.7469(38)	
α-Fe2O3+2%ZnO	5.03539(6)	13.74012(29)	
α-Fe2O3+5%ZnO	5.03688(16)	13.74552(79)	
α-Fe2O3+10%ZnO	5.03641(6)	13.74151(31)	8.42992(29)
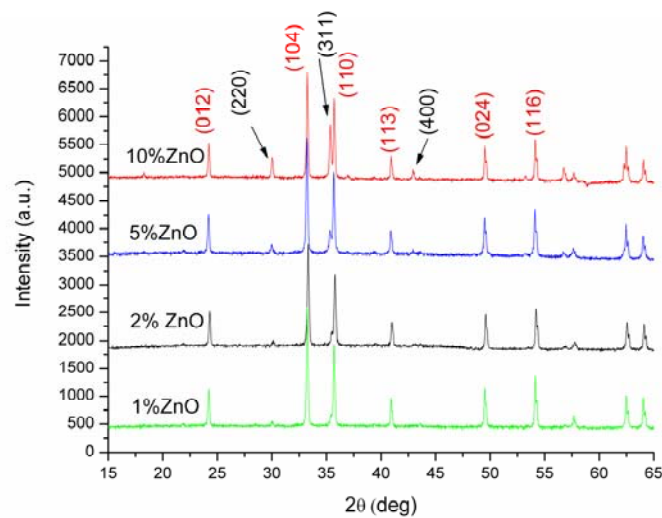
Fig. 1. X-ray diffractograms of Zn doped Fe_2O_3 sintered at 1200°C (arrows mark $ZnFe_2O_4$ spinel peaks).

Tab. II EDS analysis of α-Fe_2O_3 doped with 5 and 10 wt.% ZnO.

	Fe_2O_3 (5 wt% ZnO)			Fe_2O_3 (10 wt% ZnO)			
	zns	hm	hm	zns	zns	hm	hm
Fe	53.43	69.94	68.51	53.33	52.76	69.70	69.84
Zn	17.58			18.22	18.50		
O	28.99	30.06	31.49	28.46	28.74	30.30	30.16
Total	100	100	100	100	100	100	100

Note: hm - Fe_2O_3 zns - $ZnFe_2O_4$

_____

a)   b)
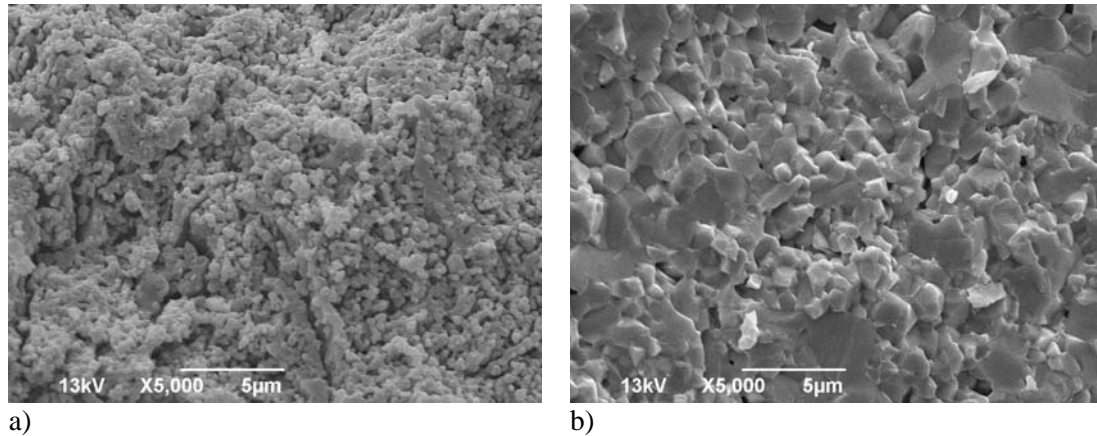
Fig. 2. SEM micrographs of Zn doped Fe_2O_3 (a) Fe_2O_3 doped with 5 wt.% ZnO, sintered at 1000^oC; (b) Fe_2O_3 doped with 10 wt.% ZnO sintered at 1100^oC.
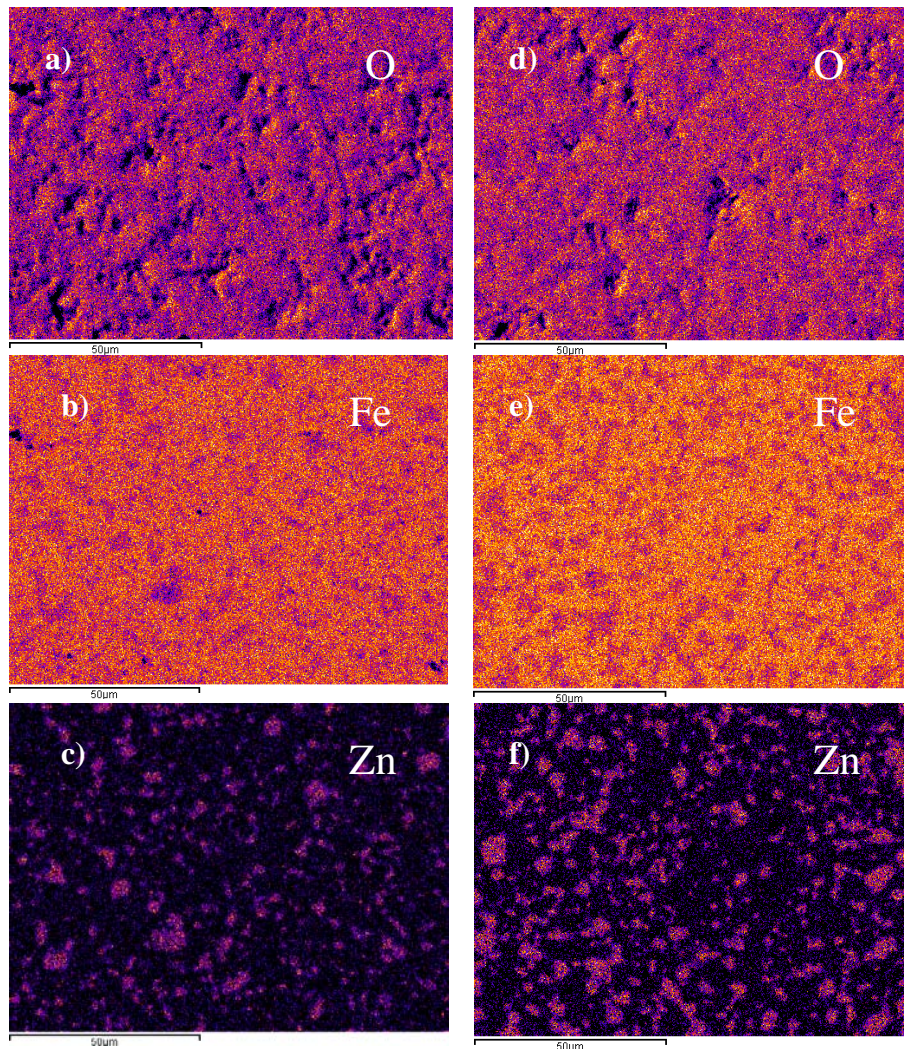
Fig. 3. X-ray elemental distribution maps of O, Fe and Zn in α-Fe_2O_3 doped with Zn in fraction of 5 wt.% (a, b and c) and 10 wt.% ZnO (d, e and f). Note: in Zn distribution maps (c and f) lighter areas are $ZnFe_2O_4$ while the darker matrix is Fe_2O_3.

_____

3.2 Electrical conductivity

The changes of electrical conductivity with temperature are shown in fig. 4. Increase in Zn doping increases electrical conductivity, thus decreasing electrical resistivity. This could be due to increased presence of the $ZnFe_2O_4$ spinel phase. According to Abdeen [17] the non-magnetic Zn ion strongly prefers the occupation of A (tetrahedral) sites in the spinel structure. The conductivity in ferrites occurs mainly due to hopping of electrons between ions of the same element existing in different valence states, distributed over crystallographically equivalent lattice sites [18]. In this case it is electron hopping between Fe^{2+} and Fe^{3+}. With formation of $ZnFe_2O_4$ the increased presence of hopping pairs is due to the presence of zinc ions in the octahedral (B) sites giving rise to electron hopping Fe^{2+}-Fe^{3+} pairs [19,20].

DC conductivity was analyzed using the Arrhenius equation [21,22]:

$$\sigma_{DC} = C \exp^{-\frac{E_\sigma}{kT}} \tag{1}$$

were C is the pre-exponential factor, E_σ is the conduction activation energy, T is the absolute temperature and k is Boltzmann's constant. The plot of log (σ_{DC}) versus (1/T) shows that this dependence is linear for all samples in a certain temperature range. Thus, for α-Fe_2O_3 samples with 1 wt.% ZnO, only the highest temperature point (498 K) does not lie on the line. For α-Fe_2O_3 samples doped with 2 wt.%, we can note a second linear dependence (marked with a dotted line in fig. 4) in the higher temperature range 423-498 K. For α-Fe_2O_3 samples doped with 5 wt.% ZnO we determined one linear dependence in the complete temperature range. For α-Fe_2O_3 samples doped with 10 wt.% ZnO we determined two linear dependencies, the first in the lower temperature range 298-373 (marked with a dotted line on fig. 4) and the second in the higher temperature range 373-498 K (marked with a full line). This indicates possible changes in the conduction mechanism. The values obtained for the conduction activation energy E_σ and pre-exponential factor using equation (1) are given in table III. If we analyze the obtained values for the conduction activation energy one can see that they are similar (between 0.423 and 0.477 eV) for the linear dependencies denoted with a full line for all analyzed samples. A lower activation energy was obtained for samples doped with 10 wt.% ZnO in the lower temperature range, while a higher value was obtained for samples doped with 2 wt.% ZnO in the higher temperature range. This shows that the amount of added Zn does to an extent influence the conduction mechanism and process activation energy. The activation energy for hematite was determined as 0.735 eV, temperature range 100-300 K [24], while the activation energy for $ZnFe_2O_4$ is much lower, and was determined as 0.19 eV for dielectric relaxation in the temperature range 290-740 K [25, 26].
Our obtained values (between 0.423 and 0.477) are in between.

Tab. III Calculated values for E_σ and C.

Sample	C $(\Omega cm)^{-1}$	E_σ (eV)
α-Fe_2O_3 + 1% ZnO	0.029	0.477
α-Fe_2O_3 + 2% ZnO	0.007	0.423
	5196[*]	0.926[*]
α-Fe_2O_3 + 5% ZnO	0.205	0.454
α-Fe_2O_3 + 10% ZnO	0.0004	0.136
	5.083[*]	0.429[*]

[*]higher temperature range

Concerning the influence of the sintering temperature, we analyzed α-Fe_2O_3 samples doped with 10 and 5 wt.% ZnO, sintered at 1100°C. The values obtained for electrical conductivity were lower than those obtained for samples with 5 and 10 wt.% ZnO 1200°C. In

_____

both cases the plot of log (σ_{DC}) versus (1/T) was linear for almost all temperatures, except for the highest (498 K) in the case of α-Fe$_2$O$_3$ samples doped with 5 wt.% ZnO and (473-498 K) for 10 wt.% ZnO, respectively. The determined activation energies were 0.458 eV and 0.404 eV, for α-Fe$_2$O$_3$ samples doped with 10 and 5 wt.% ZnO, sintered at 1100°C, respectively. These values are similar to the activation energy values obtained for samples sintered at 1200°C.
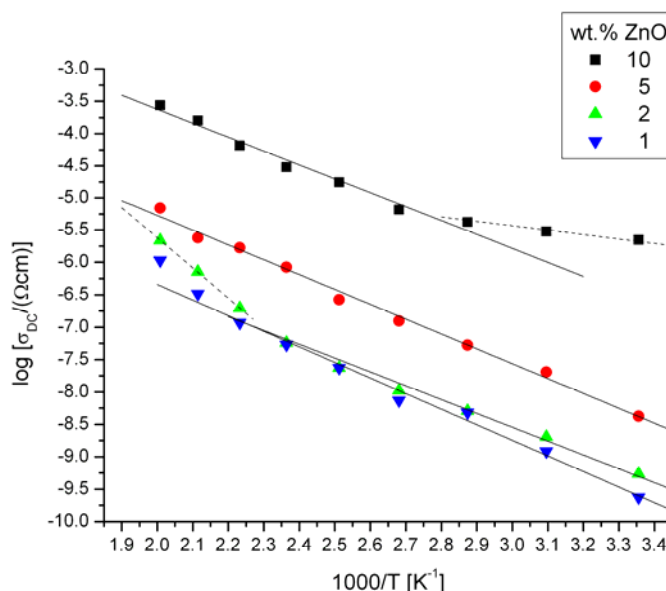
Fig. 4. Temperature dependence of DC electrical conductivity of α-Fe$_2$O$_3$ samples doped with (1-10 wt.% ZnO), sintered at 1200°C.

Mott and Davis [23] analyzed the pre-exponential factor in order to determine the conduction mechanism. If the value of C is in the range 10^3-10^4 then conduction appears in extended states, while lower values of C indicate the presence of a wide range of localization and conduction by hopping in the localized state. In our case the values of C are low indicating that conduction by hopping in localized states is the dominant mechanism, the only exception being in the higher temperature range for the sample doped with 2 wt.% ZnO.

If we assume that hopping of charge carriers is responsible for electrical conductivity then the relation between log ($\sigma_{DC}T$) and $1/T$ is linear that is consistent with the Mott model for phonon-assisted hopping of small polarons in the adiabatic limit [26]. In such a hopping process the carrier mobility is temperature dependent and the increase in dc conductivity with temperature is due to the increase in thermally activated drift mobility of charge carriers. We calculated the activation energy for the thermally activated hopping process and obtained similar values for our samples, namely 0.465, 0.487, 0.454 and 0.509 eV for α-Fe$_2$O$_3$ samples doped with 10, 5, 2 and 1 wt.% ZnO, sintered at 1200°C, and also 0.436 and 0.491 eV for α-Fe$_2$O$_3$ samples doped with 10 and 5wt.% ZnO, sintered at 1100°C.

3.3 Dielectric properties

Variation of the dielectric constant and loss tangent with frequency of Zn doped hematite samples at 323 K is shown in fig. 5. The values obtained for the dielectric constant of α-Fe$_2$O$_3$ samples doped with 10 wt.% ZnO, sintered at 1200°C are much higher than for samples doped with lower amounts of ZnO, even though the dielectric constant decreases at low frequencies and remains constant at higher frequencies. In composites the higher value of dielectric constant at low frequencies can be associated with heterogeneous conduction [27].

_____

The polaron hopping mechanism can also result in electronic polarization contributing to low frequency dispersion [28].
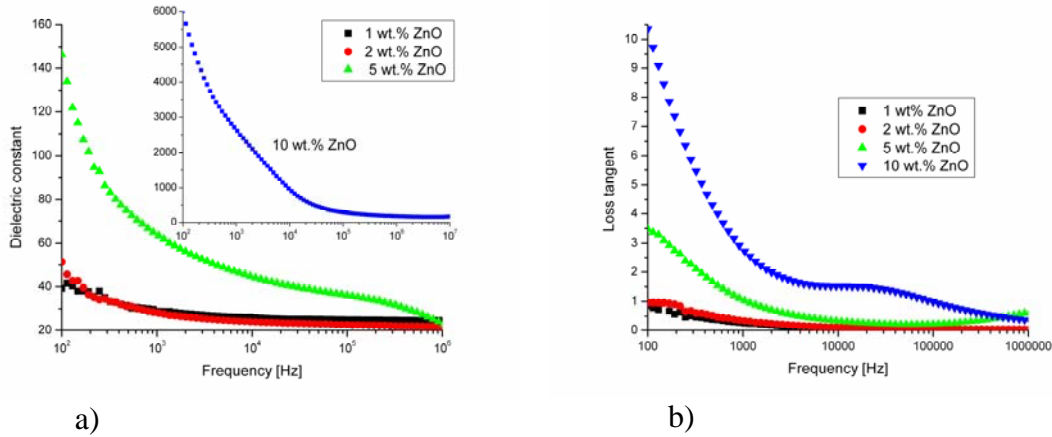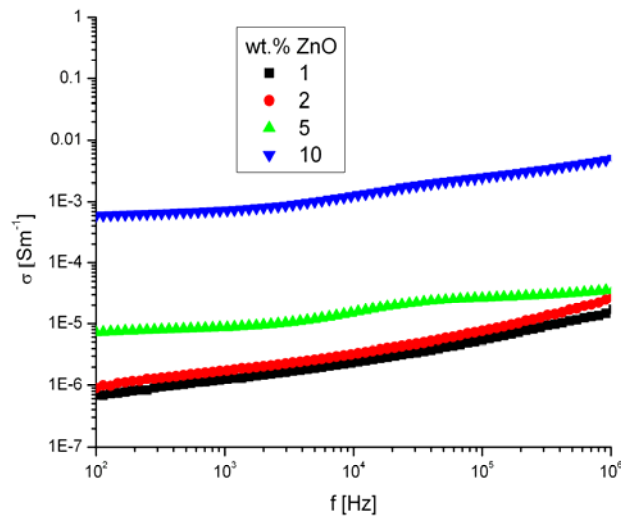

Fig. 5. Frequency dependence of the dielectric constant (a) and loss tangent (b) for Zn doped hematite samples sintered at 1200°C.
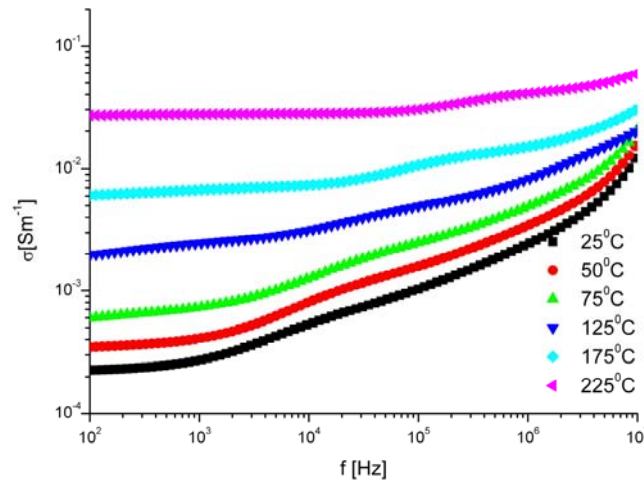
The electrical conductivity determined for α-Fe$_2$O$_3$ samples doped with Zn sintered at 1200°C is given in fig. 6. The plots are almost linear in the logarithmic scale indicating that conduction increases with increase in frequency and confirming the small polaron mechanism of conduction [27]. Changes in the electrical conductivity of an α-Fe$_2$O$_3$ sample doped with 10 wt.% ZnO, sintered at 1200°C with temperature is given in fig. 7. One can note that the sample conductivity increases with frequency and is composed of two terms [25]:

$$\sigma = \sigma_{DC}(T) + \sigma_{AC}(\omega, T) \tag{2}$$

The first term represents the temperature dependent DC electrical conductivity that we have already analyzed and is related to the drift mobility of electric charge carriers. The second term is frequency and temperature dependent and is attributed to the dielectric relaxation caused by the localized electric charge carriers and obeys the power law form. At higher temperatures the electrical conductivity increases more gently with frequency. Similar changes were noted for samples doped with smaller amounts of Zn.

Fig. 6. Electrical conductivity of α-Fe$_2$O$_3$ samples doped with Zn sintered at 1200°C.

_____

Fig. 7. Frequency dependence of electrical conductivity determined for α-Fe$_2$O$_3$ samples doped with 10 wt.% ZnO sintered at 1200°C.

3.4 Impedance analysis

Impedance data can be fitted and analyzed based on an idealized circuit model with discrete electrical components [29]. The measurements of impedance give information on resistive (real part) and reactive (imaginary part) components in a material. It can be drawn for five complex parameters such as: permittivity (ε^*), impedance (Z^*), admittance (Y^*), electric modulus (M^*) and dielectric loss tangent (tanδ) that are related to each other [29-33]:

$$\tan\delta = \varepsilon''/\varepsilon' = M''/' = Z'/Z'' = Y'/Y''. \tag{3}$$

The impedance is:

$$Z^*(\omega) = Z'(\omega) - Z''(\omega) = \left(\frac{1}{R} + j\omega C\right)^{-1} \tag{4}$$

If the simple equivalent circuit (series array of parallel RC elements) is applied where each component (grain, grain boundary and electrode-solid interface) is represented as a parallel RC element then the total complex impedance is [33]:

$$Z^*(\omega) = \left(\frac{1}{R_g} + jwC_g\right)^{-1} + \left(\frac{1}{R_{gb}} + jwC_{gb}\right)^{-1} + \left(\frac{1}{R_{el}} + jwC_{el}\right)^{-1} \tag{5}$$

where R_g, R_{gb} and R_{el} represent the grain, grain boundary and electrode-solid resistance and C_g, C_{gb} and C_{el} represent the grain, grain boundary and electrode-solid capacitance. If the electrode effects are excluded then the AC response can be modeled with two semi-circles in the impedance plane, depending on the electrical properties of the material, the first in a low frequency domain represents the resistance of grain boundary. The second one obtained in a high frequency domain corresponds to the resistance of grain or bulk properties. The resistances are calculated from the circular arc intercepts on Z' axis, while the capacitances are derived from the height of the circular arcs. The maximum value corresponds to the relaxation frequency. Typical values obtained for capacitance are in the pF range for grains, nF range for grain boundaries and above 10^{-7} for the electrode-solid capacitance [31].

If the semicircles are depressed with a center below the real axis, then the electrical response exhibits distributed impedance and a distributing factor (n) in the equivalent circuit should be taken into account. Thus a constant phase element (CPE) is introduced. A parallel combination of R, C and CPE components can be used or the CPE element can be used to

_____

replace the capacitor in each RC circuit [22, 31, 33-35]. This element is used to model the AC response of non-homogenous systems. The impedance of a CPE can be described as [33]:

$$Z_{CPE} = A^{-1}(j\omega)^{-n} \tag{6}$$

where ω is the angular frequency, A and n ($0 \leq n \leq 1$) are fitted parameters. When $n=1$, then the CPE describes an ideal capacitor with $C = A$, while when $n=0$ the CPE describes an ideal resistor with $R=1/A$.

The real value of capacitance in the case when the capacitor is replaced with a CPE element in a RC circuit can be determined as [22]:

$$C_{CPE} = (A \cdot R^{-(n-1)})^{1/n} \tag{7}$$

where R, A and n are resistance and CPE parameter values determined from the applied model, respectively. CPE elements in the equivalent circuit model have been used to describe non ideal Debye-like behavior [30] and enable taking into account phenomena occurring in the interface regions, associated with inhomogeneity and diffusion processes [22, 34, 35].

If we analyze the impedance response measured for α-Fe_2O_3 samples doped with Zn (fig. 8) it is noticeable that the impedance response includes both bulk and grain boundary effects. Depending on the amount of Zn present and also the measuring temperature these effects are more or less visible in the plots. Thus, the impedance values for samples with higher amounts of Zn (α-Fe_2O_3+10 wt.% ZnO – fig. 8a) there are two noticeable overlapping semicircles, while for samples with less Zn, and thus less $ZnFe_2O_4$ the impedance is much higher and the grain boundary effects are far more dominant and noticeable than the bulk-grain effect at high frequencies (fig. 8b).

a)   b)
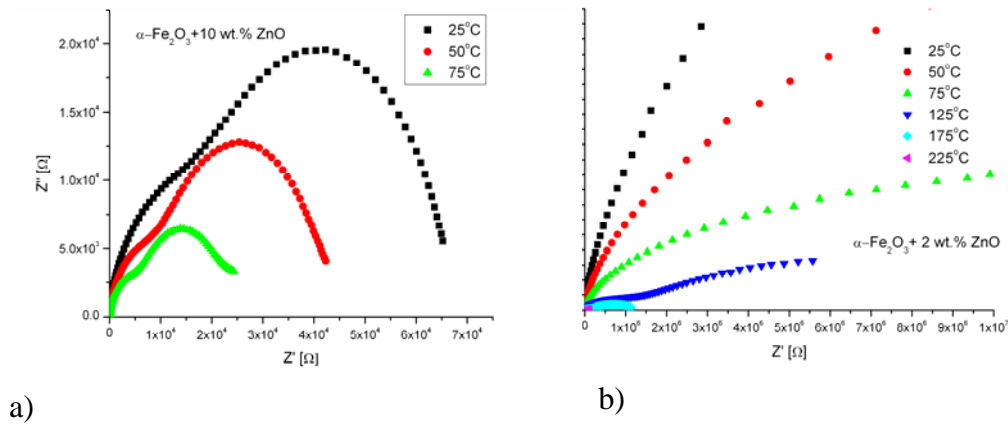
Fig. 8. Impedance response of α-Fe_2O_3 + 10 wt.% ZnO, sintered at 1200°C in the temperature range 25-75°C (a) and α-Fe_2O_3 + 2 wt.% ZnO, sintered at 1200°C in the temperature range 25-225°C (b).

Successful modeling of the impedance response (without taking into account electrode effects) was achieved using an equivalent circuit consisting of two serially connected parallel R-CPE elements taking into account grain/bulk and grain boundary effects (fig. 9). Analysis and simulation of impedance spectra was performed using EIS Spectrum Analyzer software [36]. The values determined for bulk and grain boundary components are given in table IV.

_____
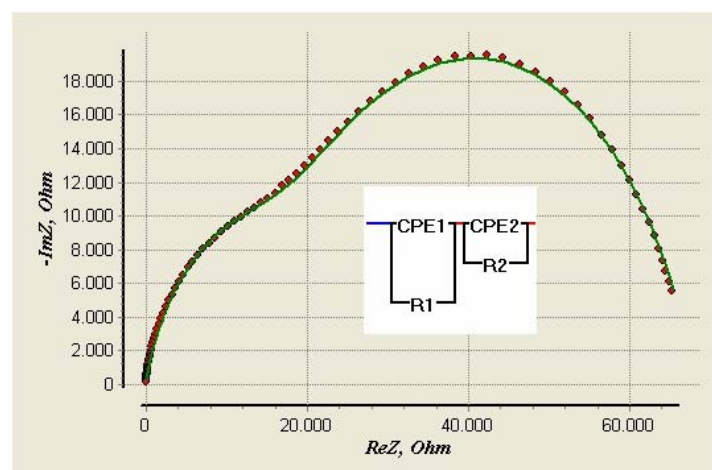
Fig. 9. Experimental (points) and calculated (solid line) complex plane impedance plots for α-Fe_2O_3 + 10 wt.% ZnO, sintered at 1200°C measured at 25°C.

**Tab. IV** Impedance parameters calculated from the complex impedance plots.

Sample	T (K)	R_g (Ω)	C_g (F)	n_g	R_{gb}(Ω)	C_{gb}(F)	n_{gb}
α-Fe_2O_3	298	1.74E4	2.23E-10	0.79	5.06E4	2.29E-9	0.79
+ 10 wt.%	323	6.93E3	2.11E-10	0.88	3.75E4	2.20E-9	0.73
ZnO	348	3.84E3	2.25E-10	0.87	2.13E4	2.91E-9	0.67
sintered	398	3.04E3	9.39E-11	0.62	3.22E3	5.92E-9	0.76
1200°C	448	1.11E3	5.75E-11	0.72	1.04E3	4.42E-9	0.83
	498	-	-	-	-	-	-
α-Fe_2O_3	298	3.08E5	3.86E-12	0.93	2.04E7	4.69E-11	0.81
+ 5 wt.% ZnO	323	-	-	-	4.47E7	5.88E-11	0.86
sintered	348	3.37E5	4.99E-12	0.99	1.44E7	3.46E-11	0.77
1200°C	398	6.63E4	5.96E-12	0.99	1.52E5	2.21E-11	0.77
	448	4.56E4	5.07E-12	0.85	-	-	-
	498	5.14E3	2.11E-11	0.79	-	-	-
α-Fe_2O_3	298	-	-	-	3.26E8	1.13E-11	0.94
+ 2 wt.% ZnO	323	1.97E7	1.86E-11	0.98	9.13E7	1.78E-11	0.92
sintered	348	1.28E7	1.41E-11	0.89	4.12E7	1.06E-11	0.83
1200°C	398	1.15E6	1.26E-11	0.90	1.12E7	2.27E-10	0.69
	448	1.39E5	1.22E-11	0.86	1.12E6	1.79E-10	0.73
	498	3.35E4	1.02E-11	0.95	8.40E4	9.31E-11	0.69
α-Fe_2O_3	298	8.66E7	8.71E-12	0.99	5.28E8	1.26E-11	0.99
+ 1 wt.% ZnO	323	4.64E7	9.17E-12	0.98	1.91E8	2.61E-11	0.99
sintered	348	1.47E7	9.51E-12	0.98	3.26E8	4.82E-11	0.94
1200°C	398	1.36E6	9.06E-12	0.97	9.11E6	1.41E-10	0.69
	448	1.92E5	9.26-E12	0.95	1.37E6	1.30E-10	0.75
	498	1.67E4	1.44E-11	0.97	1.74E5	1.02E-10	0.74

In the case of α-Fe_2O_3+10 wt.% ZnO this equivalent circuit could be applied in the temperature range 298-448 K. The values for the distributing factor for grain and grain boundary contributions (n_g and n_{gb}) are in the range between 0.6 and 0.9 that is an indication of sample inhomogeneity due to the presence of two phases (α-Fe_2O_3 and $ZnFe_2O_4$) that was previously confirmed by EDS analysis. Grain and grain boundary relaxation frequencies (ω_g

_____

and ω_{gb}) were also calculated as:

$$\omega_{max} = (A \cdot R)^{-1/n} = (C_{CPE} \cdot R)^{-1} \qquad (8)$$

where R, A and n are resistance and CPE parameter values determined from the applied model, respectively. Relaxation times τ_g and τ_{gb} were calculated as reciprocal values of grain and grain boundary relaxation peaks, respectively. The peak frequency for grain boundaries is much smaller than for grains due to their larger resistance and capacitance [37].
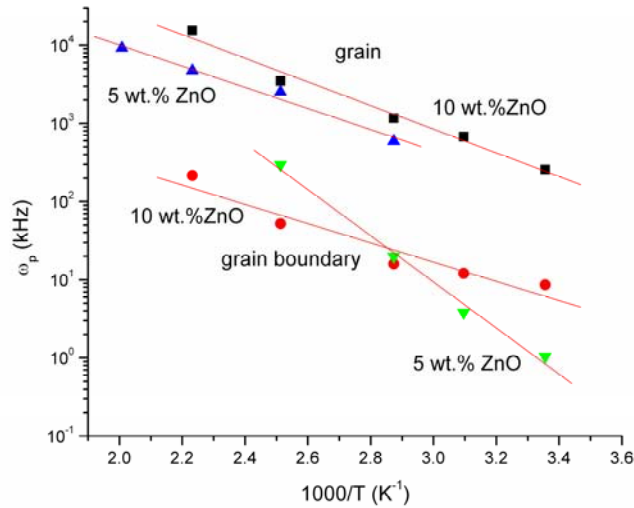
Fig. 10. Temperature dependence of the dielectric relaxation frequency ω_p for grain and grain boundary contributions for α-Fe$_2$O$_3$ + 5, 10 wt.% ZnO, sintered at 1200°C.

The temperature dependence of grain and grain boundary relaxation frequencies is shown in fig. 10. They increase with temperature (*T*) and follow an Arrhenius dependence [38]:

$$\omega_{g,gb} = \omega_0 \exp\left[-\frac{E_{g,gb}}{kT}\right] \qquad (9)$$

where ω_0 is the pre-exponential factor, $E_{g,gb}$ is the activation energy for grain and grain boundary dielectric relaxation, respectively, k is the Boltzmann constant. The determined values are given in table V.

Tab. V Activation energies determined from the relaxation frequency.

Sample	E_g (eV)	E_{gb} (eV)
α-Fe$_2$O$_3$ + 10 wt.% ZnO, 1200°C	0.299	0.244
α-Fe$_2$O$_3$ + 5 wt.% ZnO, 1200°C	0.268	0.585
α-Fe$_2$O$_3$ + 2 wt.% ZnO, 1200°C	0.567	0.618
α-Fe$_2$O$_3$ + 1 wt.% ZnO, 1200°C	0.589	0.254; 0.724[*]

[*]the first is for lower temperatures, the second is for higher temperatures

In the case of α-Fe$_2$O$_3$+5 wt.% ZnO the values of grain and grain boundary resistivity are higher. At lower temperatures the grain boundary component dominates, the grain boundary resistivity is high. At higher temperatures (448 and 498 K) we determined the grain component in the higher frequency range.

_____

In the case of α-Fe_2O_3+2 wt.% ZnO, the proposed equivalent circuit could be applied, except at room temperature where the grain boundary component dominated and the determined grain boundary resistance was very high (326 MΩ). The activation energies determined for grain and grain boundary relaxation ((temperature range 323-498 K) are given in table V.

a)   b)
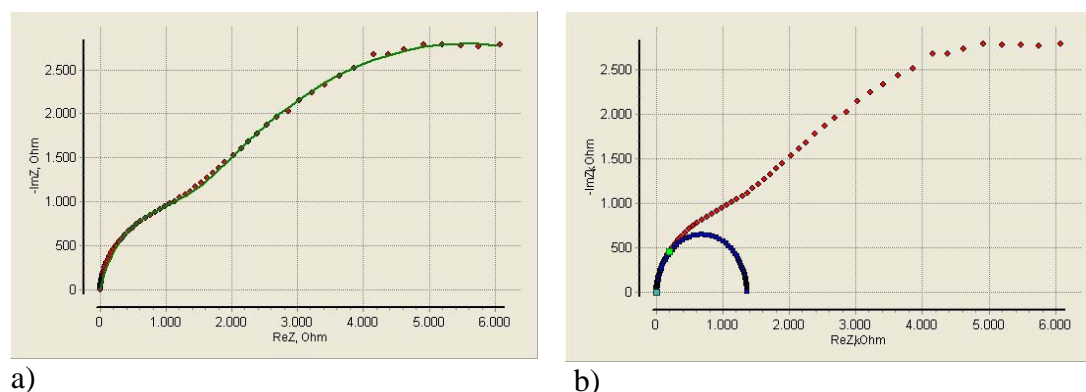
Fig. 11. Complex plane impedance plots for α-Fe_2O_3 + 1 wt.% ZnO, sintered at 1200°C measured at 125°C, experimental (points) and calculated (solid line) – (a) and determination of the grain component at high frequencies - experimental and simulated values for the grain component (b).

In the case of α-Fe_2O_3+1 wt.% ZnO the proposed equivalent circuit could be applied in the complete measured temperature range (293-498 K), though a more precise determination of the grain component was possible at higher frequencies (fig. 11). The activation energy for the grain boundary relaxation had two values, a lower one in the lower temperature range (293-348 K) and higher for (398-498 K).

4. Conclusion

In this work we have analyzed the influence of addition of different amounts of Zn on structural and electrical properties of α-Fe_2O_3. Structural analysis (XRD, SEM and EDS) revealed that addition of Zn resulted in the formation of spinel $ZnFe_2O_4$ in the form of individual grains in a α-Fe_2O_3 (hematite) matrix. Increased Zn doping lead to an increase in sample conductivity and the dielectric constant. Values of determined activation energy showed that conduction was due to electron hopping between Fe^{2+} and Fe^{3+}. Impedance data was analyzed using an equivalent circuit, enabling determination of grain and grain boundary contributions. At lower temperatures the grain boundary contribution was dominant. The lowest values of R_g and R_{gb} were obtained for samples with the highest amount of added Zn.

Acknowledgements

_____

5. References

1. M. Graetzel, Photoelectrochemical cells, Nature 414 (2001) 338-344.
2. X. C. Wang, K. Maeda, A. Thomas, K. Takanabe, G. Xin, J. M. Carlsson, K. Domen, M. Antonietti, A metal-free polymeric photocatalyst for hydrogen production from water under visible light, Nature Materials 8 (2009) 76-88.
3. J. Brillet, M. Graetzel, K. Sivula, Decoupling feature size and functionality in solution-processed, porous hematite electrodes for solar water splitting, Nano Lett. 10 (2010) 4155-4160.
4. A. Kleiman-Shwarsctein, M. N. Huda, A. Walsh, Y. Yan, G. D. Stucky, Y.-S.Hu, M. M. Al-Jassim, E. W. McFarland, Electrodeposited aluminium-doped α-Fe$_2$O$_3$ photoelectrodes: experiment and theory, Chem. Mater. 22 (2010) 510-517.
5. A. Kleiman-Shwarsctein, Y.-S. Hu, A. J. Forman, G. D. Stucky, E. W. McFarland, Electrodeposition of α-Fe$_2$O$_3$ doped with Mo or Cr as photoanodes for photocatalytic water splitting, J. Phys. Chem. C 112 (2008) 15900-15907.
6. J. A. Glasscock, P. R. F. Barnes, I. C. Plumb, N. Savvides, Enhancement of photoelectrochemical hydrogen production from hematite thin films by the introduction of Ti and Si, J. Phys. Chem. C 111 (2007) 16477-16488.
7. I. Cesar, A. Kay, J. A. Gonzales Martinez, M. Graetzel, Translucent thin film Fe$_2$O$_3$ photoanodes for efficient water splitting by sunlight: nanostructure-directing effect of Si-doping, J. Am. Chem. Soc. 128 (2006) 4582-4583.
8. W. B. Ingler, J. P. Baltrus, S. U. M. Khan, Photoresponse of p-type zinc-doped iron (III) oxide thin films, J. Am. Chem. Soc. 126 (2004) 10238-10239.
9. J. He, B. A. Parkinson, Combinatorial investigation of the effects of the incorporation of Ti, Si and Al on the performance of α-Fe$_2$O$_3$ photoanodes, ACS Comb. Sci. 13 (2011) 399-404.
10. M. N. Huda, A. Walsh,Y. Yan,S.-H. Wei, M. M. Al-Jassim, Electronic, structural and magnetic effects of 3d transition metals in hematite, J. Appl. Phys. 107 (2010)123712.
11. J. Velev, A. Bandyopadhyay, W. H. Butler, S. Sarker, Electrionic and magnetic structure of transition-metal-doped α-hematite, Phys. Rev. B 71 (2005) 205208.
12. S. S. Shinde, R. A. Bansode, C. H. Bhosale, Physical properties of hematite α-Fe$_2$O$_3$ thin films: application to photoelectrochemical solar cells, J. Semicond. 32 (2011) 013001.
13. M. A. Valenzuela, P. Bosch, J. Jimenez-Becerrill, O. Quiroz, A. L. Paez, Preparation, characterization and photocatalytic activity of ZnO, Fe$_2$O$_3$ and ZnFe$_2$O$_4$, J. Photochem. Photobiol. A 148 (2002) 177-182.
14. Y. Shen, X. Y. Li, Q. D. Zhao, Y. Hou, M. Tade, S. M. Liu, Facile synthesis and characterization of ZnFe$_2$O$_4$/α-Fe$_2$O$_3$ composite hollow nanospheres, Mater. Res. Bull. 46 (2011) 2235-2239.
15. A. Le Bail, H. Duroy, J. L. Fourquet, Ab-inition structure determination of LiSbWO$_6$ by X-ray powder diffraction, Mater. Res. Bull. 23 (1988) 447-452.
16. J. Rodriguez-Carvajal, Recent advances in magnetic structure determination by neutron powder diffraction, Physica B 192 (1993) 55-69.
17. A. M. Abdeen, Dielectric behaviour of Ni-Zn ferrites, J. Magn. Magn. Mater. 192 (1999) 121-129.
18. G. Stojanovic, V. Srdic, M. Maletin, Electrical properties of yttrium-doped Zn and Ni-Zn ferrites, Phys. Status Solidi A 10 (2008) 2464-2468.
19. B. Baruwati, K. M. Reddy, S. V. Manorama, R. K. Singh, O. Parkash, Tailored conductivity behavior in nanocrystalline nickel ferrite, Appl. Phys. Lett. 85 (2004) 2833-2835.

_____

20. E. Veena Gopalan, K. A. Malini, S. Sagar, D. Sakthi Kumar, Y. Yoshida, I. A. Al-Omari, M. R. Anantharaman, Mechanism of ac conduction in nanostructured manganese zinc mixed ferrites, J. Phys. D: Appl. Phys. 42 (2009) 165005.

21. T. Ivetic, M. V. Nikolic, M. Slankamenac, M. Zivanov, D. Minic, P. M. Nikolic, M. M. Ristic, Influence of Bi_2O_3 on microstructure and electrical properties of $ZnO-SnO_2$ ceramics, Sci. Sintering 39 (2007) 229-240.

22. M. Slankamenac, T. Ivetic, M. V. Nikolic, N. Ivetic, M. Zivanov, V. B. Pavlovic, Impedance response and dielectric relaxation in liquid-phase sintered $Zn_2SnO_4-SnO_2$ ceramics, J. Electron. Mater. 39 (2010) 447-455.

23. N. F. Mott, E. A. Davis, Electronic Processes in Non-Crystalline Materials, Oxford, UK Clarendon, 1979.

24. N. Guskos, G. J. Papadopoulos, V. Likodimos, S. Patapis, D. Yarmis, A. Przepiera, J. Majszczyk, J. Typek, M. Wabia, K. Aidinis, Z. Drazek, Photoacoustic, EPR and electrical conductivity investigation of three synthetic mineral pigments: hematite, goethite and magnetite, Mater. Res. Bull. 37 (2002) 1051-1061.

25. A. M. Abdeen, Electric conduction in Ni-Zn ferrites, J. Magn. Magn. Mater. 185 (1998) 199-206.

26. N. F. Mott, Conduction in glasses containing transition metal ions, J. Non-Cryst. Solids 1 (1968) 1-17.

27. Z. Yu, C. Ang, Maxwell-Wagner polarization in ceramic composites $BaTiO_3$-$(Ni_{0.3}Zn_{0.7})Fe_{2.1}O_4$, J. Appl. Phys. 91 (2002) 794-797.

28. S. S. Shinde, C. H. Bhosale, K. Y. Rajpure, Studies on morphological and electrical properties of Al incorporated combusted iron oxide, J. Alloys Compd. 509 (2011) 3943-3951.

29. S. Kumar, K. M. Batoo, R. Prakash, H. K. Choi, B. H. Koo, J. I. Song, H. Chung, H. Jeong, C. G. Lee, Impedance spectroscopic study on $Mn_{1+x}Fe_{2-2x}Ti_xO_4$ $(0 \le x \le 0.5)$ ferrites, J. Cent. South Univ. Technol. 17 (2010) 1133-1138.

30. A. R. West, D. C. Sinclair, N. Hirose, Characterization of electrical materials, especially ferroelectrics, by impedance spectroscopy, J. Electroceramics 1 (1997) 65-71.

31. E. J. Abram, D. C. Sinclair, A. R. West, A strategy for analysis and modeling of impedance spectroscopy data of electroceramics: doped lanthanum gallate J. Electroceramics 10 (2003)165-177.

32. R. Gerhardt, Impedance and dielectric spectroscopy revisited: distinguishing localized relaxation from long-range conductivity, J. Phys. Chem. Solids 55 (1994) 1491-1506.

33. R. Martinez, A. Kumar, R. Palai, J. F. Scott, R. S. Katiyar, Impedance spectroscopy analysis of $Ba_{0.7}Sr_{0.3}TiO_3/La_{0.7}Sr_{0.3}MnO_3$ heterostructure, J. Phys. D: Appl. Phys. 44 (2011) 105302.

34. F. D. Morrison, D. J. Jung, J. F. Scott, Constant-phase-element (CPE) modeling of ferroelectric random-access memory lead zirconate-titanate (PZT) capacitors, J. Appl. Phys. 101 (2007) 094112.

35. E. Thirumal, D. Prabhu, K. Chattopadhyay, V. Ravichandran, Synthesis, magnetic and electrical properties of Fe-containing SiO_2nanocomposite, J. Alloys. Compd. 502 (2010) 169-175.

36. A. S. Bondarenko, G. Ragoisha, EIS Spectrum Analyzer, http://www.abc.chemistry.bsu.by

37. K. M. Batoo, S. Kumar, C. G. Lee, Alimuddin, Study of ac impedance spectroscopy of Al doped $MnFe_{2-2x}Al_xO_4$, J. Alloys. Compd. 480 (2009) 596-602.

38. N. Ponpandian, P. Balaya, A. Narayanasamy, Electrical conductivity and dielectric behaviour of nanocrystalline $NiFe_2O_4$ spinel, J. Phys.:Condens. Matter 14 (2002) 3221-3237.

_____

Садржај: *Проучени су ефекти допирања цинком на диелектрична и електрична својства α-Fe₂O₃ хематита. Рентгенска дифракциона анализа је показала присуство две фазе у свим узорцима: хематита и спинела ZnFe₂O₄, при чему се количина присутног спинела увећавала са порастом садржаја Zn. Скенирајућа електронска микроскопска анализа у комбинацији са ЕДС анализом је показала да је фаза са цинком присутна у виду индивидуалних спинелних зрна ZnFe₂O₄ у матрици хематита. ДЦ проводност је мерена у температурном интервалу 25-225ºC (298-498К). Мерења импедансне спектроскопије у истом температурном интервалу су извршена у фреквентном опсегу 100 Hz-10MHZ. Увећање садржаја Zn је довело до повећања електричне проводности и вишим вредностима диелектричне константе. Отпорност и капацитивност зрна и граница зрна су анализиране моделовањем експерименталних резултата коришћењем еквивалентног кола.*
Кључне речи: *Рентгенска дифракција, СЕМ, диелектрични одговор, електрични транспорт.*